Automatic Detection of Dispersed Defects in Resin Eyeglass Based on Machine Vision Technology

WEI DING [1,2], **QINGGUO WANG** [2], **AND JIANFENG ZHU** [3]
[1]Faculty of Electrical Engineering and Automation, Changshu Institute of Technology, Changshu 215500, China
[2]Faculty of Engineering and the Built Environment, Institute for Intelligent Systems, University of Johannesburg, Johannesburg 2006, South Africa
[3]School of Mechanical Engineering, Jiangsu University, Zhenjiang 212013, China

Corresponding author: Wei Ding (dingwei@cslg.edu.cn)

ABSTRACT This paper is concerned with detection of dispersed defects in the resin eyeglass. At present, manual detection is always used in industry, which inevitably causes impairing eyes and a high rate of false-negative detection. Statistics show that its average accuracy and the average detection time are about 85% and 10s, respectively. We for the first time propose an automatic approach to detection of dispersed defects in resin eyeglass, based on the machine vision technology. It is observed that the refractivity of the normal and the defective regions of an eyeglass are different, and thus the reflection image is also collected in our system in addition to the normal transmission image. Such an optical imaging system is modelled and its analysis shows the gray-scale gradient difference between the normal and defective regions in the acquired image is dramatically enhanced under the illumination of a point light source with our designed system. An image processing algorithm is then developed to reveal the above difference and detect dispersed defects in resin eyeglasses. Our simulation study verifies the proposed approach. Further, its experimental evaluation was carried out and the result was consistent with the simulation one, showing that its detection accuracy and the average detection time were 97.50% and 0.636s, respectively, which meet the requirements for online detection of dispersed defects.

INDEX TERMS Automatic detection, dispersed defects, imaging analysis, machine vision, resin eyeglass.

I. INTRODUCTION

It is predicted in [1] that by 2050 there will be 4758 million people with myopia and 938 million people with high myopia, accounting for 49.8% and 9.8% of the population in the world, respectively. As wearing eyeglasses is an effective way to correct visual acuity, a great demand for eyeglass is expected. Due to the low density, impact resistance, strong light transmission, low cost and high plasticity, the thermoplastic resin is the most commonly used material of eyeglass [2], [3]. The defect detection is an essential task in the manufacture of resin eyeglass, because the unqualified eyeglasses are inevitable, which not only fail to help the wearers but also cause damages to eyes. The dispersed defects, which

are caused by the inhomogeneous material and temperature during the curing process, are with the characteristic of transparency, variety and internality. In manufacture, the eyeglass with dispersed defects is discarded, the detection of which at present depends on the human eye. The inspectors search for defects by their naked eyes throughout the eyeglass. This way is of the following shortcomings. First, eyes of inspectors may be damaged severely, since they need to work more than 8 hours in the environment of a high light intensity, per day. Second, the detection accuracy is in general less than 85% that is not satisfactory. One of the reasons is that some minor defects cannot be found by humans, because the minimum distance between two points that can be identified by naked eyes needs to be more than 0.1 mm. Third, the efficiency is not controllable, which depends on the experience or even emotion of the inspector. Therefore, automatic detection is

The associate editor coordinating the review of this manuscript and approving it for publication was Haiyong Zheng [ID].

urgently needed. To the best knowledge of the authors, until now, no research on automatic detection methods for dispersed defects in resin eyeglass has been carried out.

Machine vision is an effective technology to support online defect detection [4]–[6], and the existing relevant work focuses mainly on detection of defects on optical components made of glass and resin. Various technologies have been developed to detect defects on optical components made of glass. The first research was conducted in Lawrence Livermore national laboratory (LLNL) in the United States in 1995. As a result, by using the uniformly illuminated volume through the edge of the detected large-scale optics, bulk defects scatter some of this light and thus are visible by photographic imaging [7], [8]. In recent years, Deng *et al.* [9] developed a defect detection system with a sort of structured illumination that realized automatic detection of transparent micro defects on the polymeric polarizer. Kuo *et al.* [10] further proposed a high precision automatic detection system for the classification of four classes of defects in polarizing film (e.g., dents, inclusions, spots and scratches), and the accuracy was 98.9% with detection time for one single image of 2.57 s. Yuan *et al.* [11] utilized the transmission imaging technology and a neural network to classify and segment the defects on the screen of the mobile phone with the maximum error of 40 um. With the reflection imaging method combined with the line-scan camera, Chang *et al.* [12] developed a defect detection system for the touch screen. The detection accuracy for bubbles, cracks, scratches and edge damages on the screen was 94%.

Despite some similar characters of defects in glass and resin (e.g., shape and transparency), their optical properties are quite different (e.g., diffraction, interference, reflection and refraction), such that the above-mentioned imaging methods cannot be applied for detection of defects in resin. At present, the research on defect detection for resin components concentrates only on point defects and linear defects generated during processing, cleaning and transferring; see for instance [13]–[16]. In particular, a detection method for certain defects in the resin eyeglass was proposed by Hongbing [17]. Nevertheless, the patterns of point and linear defects are quite different from those of the dispersed defects studied in this paper. Therefore, the aforementioned methods are not completely suitable for detection of dispersed defects in resin eyeglass.

To the best knowledge of the authors, until now the problem of how to automatically detect dispersed defects in resin eyeglass still remains open. A solution is for the first time provided in this paper based on the machine vision technique. More specifically, the methods of transmission imaging and reflection imaging are combined to build an optical imaging system. It is observed that the refractivity of the normal region and the defective region is different, causing differences of the optical characters, e.g., the light path and power. This fact is considered for detection. In this way, an image of the dispersed defect with high contrast is obtained. The simulation results on the imaging system show that the contrast between the normal and defective regions is clearly presented under the illumination of a point light source: the density of rays in the dispersed defect region is 1.13%, and that in the normal region is 6.64%. The experimental results show that with the designed image-processing algorithm used, the detection accuracy and the average detection time are 97.50% and 0.636s, respectively, both of which satisfy the requirements for online detection of dispersed defects.

The remainder of this paper is organized as follows. The imaging mechanism and the method of the image processing are presented in Section II. According to this imaging mechanism, the optical imaging system is developed and simulated in Section III. An experimental setup is built to demonstrate the effectiveness of the proposed method of automatic detection of dispersed defects in the Section IV. Section V concludes this paper.

II. THE PROPOSED APPROACH

Thus far, a variety of methods to detect defects in optical components have been reported in the literature; see for instance [4]–[17]. However, images of dispersed defects studied in this paper cannot be acquired by the existing approaches, because the optical properties and patterns between the studied defects and other types of defects are quite different. To achieve detection, the difference between the normal region and the defective region of the eyeglass needs to be exploited. Specifically, the difference in material density results in the loss of the optical uniformity of the eyeglass with dispersed defects [18], leading to differences of some optical characters such as refractivity. On the basis of the above finding, an optical imaging system is designed for detection, in which the transmission imaging with reflection imaging are combined. This system is shown in Fig. 1 and explained as follows. The optical imaging system is illuminated with the point light source; then the image of the defective eyeglass is projected
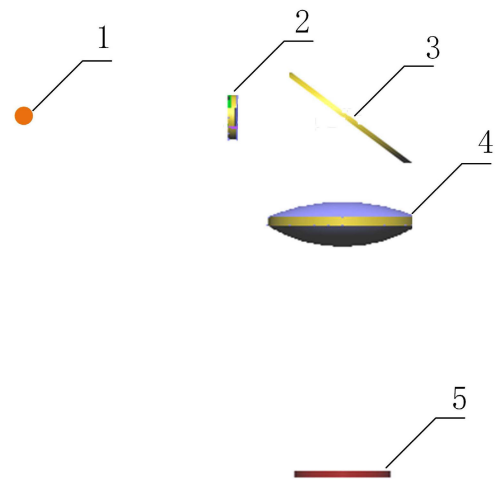

FIGURE 1. Design of an optical imaging system. 1. Light source; 2. Detected defective eyeglass; 3. Folding mirror; 4. Imaging convex lens; 5. Image receiver.
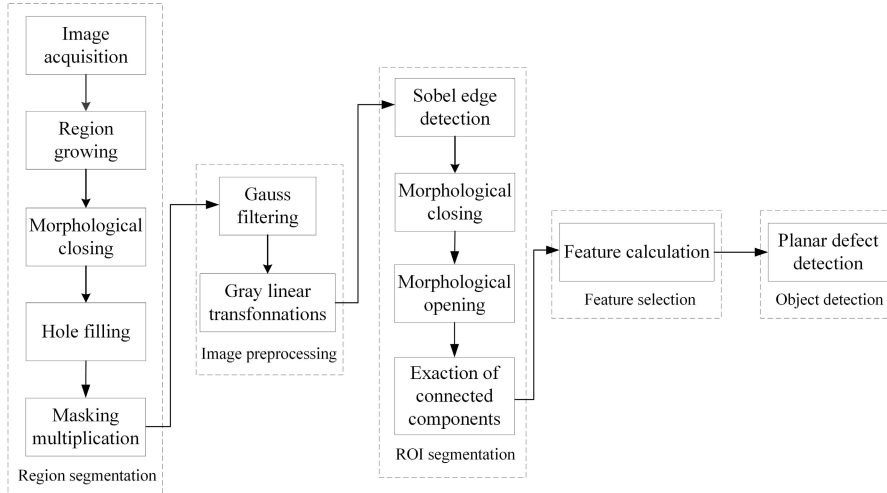
FIGURE 2. The flow chart of image processing algorithm for dispersed defects detection.

on the imaging receiver by the transmission imaging; next the image is acquired by the camera through reflection imaging. The light source is located at the origin of the imaging system, whose luminous flux Φ needs to satisfy $\Phi \geq \overline{\Phi}$ with $\overline{\Phi} > 0$ a threshold ensuring that a clear image is obtained.

The acquired image of the defective eyeglass is characterized [19] by the following matrix:

$$F = \begin{bmatrix} f(1,1) & f(1,2) & \cdots & f(1,N) \\ f(2,1) & f(2,2) & \cdots & f(2,N) \\ \vdots & \vdots & \ddots & \vdots \\ f(M,1) & f(M,2) & \cdots & f(M,N) \end{bmatrix},$$

where $f(x,y) \in [0, 255]$ denotes the gray-scale value at the point (x, y), $x = 1, 2, \cdots, M$, $y = 1, 2, \cdots, N$.

The difference in refractivity of the defective eyeglass leads to different ray densities of the transmission light on the imaging receiver. This further causes difference in gray-scale gradients in the acquired image. Between any two points (x_p, y_p) and (x_q, y_q) in the region of the eyeglass R, such a diversity is determined by

$$\left| \tau_m(x_p, y_p) - \tau_m(x_q, y_q) \right| \geq \overline{\tau}_m,$$

where $p \neq q$, $\tau_m(\cdot, \cdot)$ denotes the gray-scale gradient at $(\cdot, \cdot)$.

An image processing algorithm with high efficiency and robustness is given for detection of dispersed defects [20]. It mainly includes region segmentation, image preprocessing, region of interest (ROI) segmentation, feature selection and object detection. The flow chart of image processing algorithm is displayed in Fig. 2.

The acquired image of the defective eyeglass contains the complex background (e.g., the eyeglass support and the imaging plate) and noise. Since the background and noise affect the result of $\left| \tau_m(x_p, y_p) - \tau_m(x_q, y_q) \right|$, they need to be removed. The removal of the background is achieved via region growing, morphological closing, hole filling, morphological opening and masking multiplication. The region

growing [21] is one of region-based segmentation algorithms, which groups pixels or subregions into larger regions based on the predefined criteria.

Due to a distinct difference between the gray-scale value of the eyeglass region and that of the background, the region growing is used to pre-segment the region of eyeglass in the image. Meanwhile, in order to reduce the dependence of the segmentation result on the seed point, the growing criteria based on the gray-scale difference of the region is adopted. The usage is presented as follows. Firstly, choose one point in F as the initial seed point. This point and its neighborhood form a set denoted by Ω_1 with $m \times n$ elements. The element is denoted by (x_a, y_b) with $a = 1, \cdots, m$ and $b = 1, \cdots, n$, which is extracted if its gray-scale difference is less than a threshold ε, i.e.,

$$A_1 = \left\{ (x_a, y_b) \mid |f(x_a, y_b) - \overline{C}_1| \leq \varepsilon \right\}, \tag{1}$$

where $\overline{C}_1 = \frac{1}{m \times n} \sum_{(x_a, y_b) \in \Omega_1} f(x_a, y_b)$. Assume A_1 has n_1 elements. Each element is regarded as a new seed point, and its neighborhood and itself form a new set denoted by $\Omega_{2,j}, j \in \{1, \cdots, n_1\}$. Repeat operation (1) to extract eligible elements from $\Omega_{2,j}$, with the resulting set denoted by $A_{2,j}$, $j = 1, \cdots, n_1$. Define

$$B_1 = A_1,$$
$$B_2 = A_1 \cup A_{2,1} \cup \cdots \cup A_{2,n_1}.$$

The total number of the elements in $A_{2,1}, \cdots, A_{2,n1}$ is denoted by n_2. Each element is seen as a new seed point again to determine the corresponding set $\Omega_{3,j}, j \in \{1, 2, \cdots, n_2\}$. Then operation (1) is conducted to obtain B_3. The above steps are performed recursively, until $B_i = B_{i+1}, i \in \{1, 2, 3, \cdots\}$. In the meantime, B_i is denoted by $\overline{B}$. A new binary image $\overline{F}_1$ is defined by $\overline{F}_1 = (\overline{f}_1(x, y))$, where

$$\overline{f}_1(x, y) = \begin{cases} 1, & \text{if } (x, y) \in \overline{B}, \\ 0, & \text{otherwise.} \end{cases}$$

The morphological closing [22] is defined by

$$E(P, Q) = (P \oplus Q) \ominus Q, \tag{2}$$

where P is a binary matrix with 1 representing the foreground and 0 denoting the background; Q is a matrix consisting of the structuring elements that are chosen by the designer; $\oplus$ stands for the morphological dilation operation; and $\ominus$ represents the morphological erosion operation. The morphological closing is able to smooth the contour of an object, fuse narrow breaks and long thin gulfs, eliminate small holes and fill gaps in the contour. Due to the difference between different foregrounds, the selection of Q is not unique in the subsequent designs, such as Q_i, $i = 1, 2, 3, \cdots$. After region growing, the dispersed defects adjacent to the contour of R may be considered as the background and thus removed. To achieve this, operation (2) is carried out as $E_1(\overline{F}_1, Q_1)$ to fill gaps in the contour of $\overline{B}$, where Q_1 is a rectangular structuring element with width 20 pixels and height 10 pixels.

The dust and defects, which are strictly within $\overline{B}$, change the gray-scale value of the corresponding pixels and cause information loss in the image of $\overline{F}_1$. Therefore, the hole filling algorithm [23] begins with a point S_l, $l \in \{1, 2, \cdots, \alpha\}$ inside the 8-connected boundary $D = E_1 - (E_1 \ominus Q_2)$ of the lost regions, until one of the entire lost region within $\overline{B}$ is extracted, as shown below

$$X_k = (X_{k-1} \oplus Q_3) \cap D^c, \quad k = 1, 2, \cdots, \Psi, \tag{3}$$

where $X_0 = S_1$; D^c is the complementary set of D; and $Q_3 \in R^{3 \times 3}$ is a symmetric structuring element. If $X_k = X_{k-1}$, then we make $\overline{X}_1 = X_k$ as the first lost region and $k = \Psi$. Then repeat operation (3) with $X_0 = S_2$ to extract the second lost region $\overline{X}_2$. The above steps are performed with the rest of points S_l, $l \in \{3, 4, \cdots, \alpha\}$ recursively. Thus, a binary matrix with 1 representing the region of eyeglass and 0 denoting the background is acquired after filling all the lost regions, which is given by

$$H_1 = \overline{X}_1 \cup \overline{X}_2 \cup \cdots \cup \overline{X}_\alpha \cup D \cup E_1. \tag{4}$$

The acquired image of the defective eyeglass without background is characterized by

$$H_2 = FH_1. \tag{5}$$

The noise in the image is with a similar gray-scale gradient to the dispersed defect, thus interfering the detection result. To reduce this effect, a gaussian filter of size $(2u+1) \times (2v+1)$ is employed. The filtered output of point (x, y) is given [24] by

$$h_3(x, y) = \frac{\sum_{s=-u}^{u} \sum_{t=-v}^{v} h_2(x+s, y+t) \frac{1}{2\pi\sigma^2} e^{-\frac{s^2+t^2}{2\sigma^2}}}{\sum_{s=-u}^{u} \sum_{t=-v}^{v} \frac{1}{2\pi\sigma^2} e^{-\frac{s^2+t^2}{2\sigma^2}}}, \tag{6}$$

where σ is the standard deviation of the distribution, and $h_2(\cdot, \cdot)$ denotes the gray-scale value at $(\cdot, \cdot)$ in H_2. To generate a complete filtered image $H_3 = (h_3(x, y)) \in R^{M \times N}$, operation (6) is used for all $x = 1, 2, \cdots, M$ and $y = 1, 2, \cdots, N$.

To further enhance the contrast between the normal and defective regions in H_3, the following gray linear transformation [25] is conducted:

$$h_4(x, y) = \frac{256(h_3(x, y) - h_{3min})}{h_{3max} - h_{3min}}, \tag{7}$$

where h_{3min} and h_{3max} are the minimum and maximum gray-scale values of H_3, respectively, both of which are within the range of [0, 255].

According to the gray-scale gradient difference between the normal region and the defective region, the sobel edge detection algorithm [26] is adopted to detect the edges of dispersed defects in the image. By using mask of size 3×3, gray-scale gradients at (x, y) are approximately defined as follows:

$$\begin{aligned} \tau(x, y)_x &= h_4(x+1, y-1) + 2h_4(x+1, y) \\ &\quad + h_4(x+1, y+1) - h_4(x-1, y-1) \\ &\quad - 2h_4(x-1, y) - h_4(x-1, y+1), \\ \tau(x, y)_y &= h_4(x-1, y+1) + 2h_4(x+1, y) \\ &\quad + h_4(x+1, y+1) - h_4(x-1, y-1) \\ &\quad - 2h_4(x, y-1) - h_4(x+1, y-1). \end{aligned}$$

The magnitude of the gray-scale gradients is given by

$$\tau_m(x, y) = \sqrt{\tau(x, y)_x^2 + \tau(x, y)_y^2}. \tag{8}$$

The edge of the dispersed defect candidate in the image is selected by

$$H_5 = \{(x, y) | \overline{\lambda}_1 \le \tau_m(x, y) \le \overline{\lambda}_2\}, \tag{9}$$

where $\overline{\lambda}_1$ and $\overline{\lambda}_2$ are the lower and upper thresholds, respectively. The new binary image is expressed by $\overline{F}_2 = (\overline{f}_2(x, y))$, where

$$\overline{f}_2(x, y) = \begin{cases} 1, & \text{if } (x, y) \in H_5, \\ 0, & \text{otherwise.} \end{cases}$$

Due to the discontinuity of the edges in $\overline{F}_2$, the dispersed defect may be separated into several parts. Therefore, operation (2) is conducted for connection, yielding $E_2(\overline{F}_2, Q_4)$, where Q_4 is a rectangular structuring element with width 5 pixels and height 1 pixel.

The opening operation [27] is able to smooth the contour of an object as well. Opposed to the closing operation, the opening operation is capable of breaking narrow isthmuses and eliminating thin protrusions. To make the outline smooth and remove invalid connections, the following opening operation is conducted:

$$H_6 = (E_2 \ominus Q_5) \oplus Q_5, \tag{10}$$

where Q_5 is a circular structuring element with radius 1 pixel. In this way, the regions of the dispersed defect candidates H_6 are determined.

A method of extracting connected components [28] is used to connect pixels that are assigned to the same object. To extract the θ-th connected component $\overline{P}_\theta$ in the image,
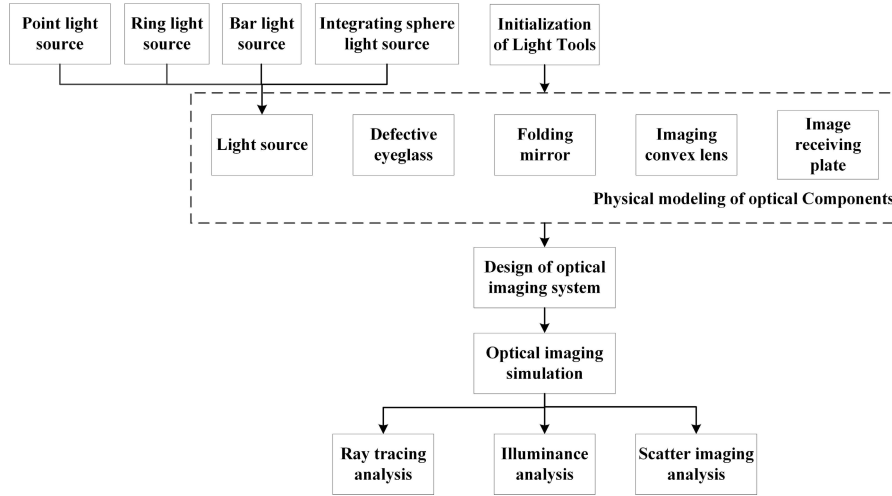
FIGURE 3. Optical imaging simulation flow chart.

$\theta \in \{1, 2, \cdots, \Theta\}$, the following algorithm is carried out with a point $P_0 = U_1$ in one of the connected component contained in H_6:

$$P_\xi = P_{\xi-1} \oplus Q_3 \cap H_6, \quad \xi = 1, 2, \cdots, \Xi. \tag{11}$$

If $P_\xi = P_{\xi+1}$, then $\overline{P}_1 = P_\xi$ and $\xi = \Xi$. Subsequently, repeat operation (11) with $P_0 = U_2$ to extract $\overline{P}_2$. The above steps are performed with the rest of points $U_\theta, \theta \in \{3, 4, \cdots, \Theta\}$ recursively.

Since it is not true that $\overline{P}_\theta, \theta = 1, 2, \cdots, \Theta$ are all dispersed defects, the eccentricity, the ratio of area and the number of dispersed defects are chosen as classification features. The eccentricity is defined by $E_{cc} = R_a/R_b$, where R_a and R_b are the major and minor radiuses of the equivalent ellipses, respectively. The ratio of area is defined as $R_x = V_{pmax}/V_{sum}$, where V_{pmax} is the area of the maximum connected component, and V_{sum} is the area of the eyeglass region. The eyeglass is deemed to be defective if one or more of the following hold

$$M > \overline{M}, \tag{12}$$
$$R_x > \overline{R}_x, \tag{13}$$
$$V_\theta > \overline{V}, \ E_{cc\theta} > \overline{E}, \ \theta \in \{1, 2, \cdots, \Theta\}, \tag{14}$$

where M is the number of the connected components with $E_{cc} > \overline{E}$; $\overline{M}, \overline{A}$ and $\overline{E}$ are positive thresholds; $\overline{R}_x$ is the ratio threshold between V_{pmax} and V_{sum}; and V_θ is the area of the θ-th connected component.

III. SIMULATION STUDY

A. SIMULATION ENVIRONMENT
The above-mentioned optical imaging system for detection of dispersed defects is simulated on the software of Light Tools [29] composed of the point light source, the defective eyeglass, the folding mirror, the imaging convex lens, and the image receiver, as shown in Fig. 1. The optical imaging simulation flow of dispersed defects is exhibited in Fig. 3

and explained as follows. Firstly, each optical component in the imaging system is modeled. Then, an imaging system is designed for dispersed defect detection based on the refractivity difference between the normal and defective regions on the resin eyeglass. Finally, the developed imaging system is simulated with ray-tracing analysis, scatter distribution analysis and illuminance analysis [30].

In the simulation, the Poly (methyl methacrylate) (PMMA) and the polycarbonate (PC) are selected as the materials of the normal region and the defective region of the eyeglass, respectively. The 300-degree concave myopia eyeglass is selected as the detection object, with the radius of the front surface, the radius of the back surface, the thickness, the focal length and the diameter being 40 cm, 39 cm, 0.7 cm, 39.9 cm and 8 cm, respectively. The physical model of the resin eyeglass with a dispersed defect is shown in Fig. 4.
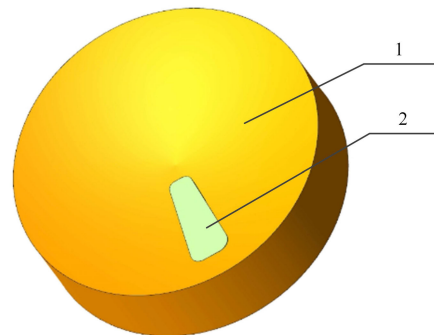

FIGURE 4. The physical model of resin eyeglass with dispersed defect. 1. Normal region; 2. Defect.

The folding mirror is selected as the white imaging screen to reflect the transmission image of the defective eyeglass to the camera. The optical property of the folding mirror is smooth optics with reflectivity of 100%. The imaging convex lens, playing a role of camera lens, is used to capture and

converge the reflected light from the folding mirror. The parameters of the folding mirror and the imaging convex lens are given in Table 1. The image receiver serves as the imaging chip of the CCD camera to collect the captured image and calculate the gray-scale values, the illumination and the number of rays with the graphical output for the subsequent data analysis.

TABLE 1. Parameters of folding mirror and imaging convex lens.

Parameter	Value
Type	FMir2
Taper	1
Radius of the folding mirror	4 cm
Radius of the imaging convex lens	10 cm
Curvature radius of the front surface	20 cm
Curvature radius of the rear surface	15 cm

B. SIMULATION RESULT

With the optical imaging system applied for the defective eyeglass, the simulation result is exhibited in Fig. 7(a). As seen, the image of the defect shown in Fig. 4 is successfully obtained. Therefore, the simulation result verifies the effectiveness of the designed defect detection scheme.

Note the fact that different light sources yields different imaging effects. Therefore, some tests on the optical imaging system are carried out with other three types of light sources, i.e., the ring light source, the integrating sphere light source and the bar light source. The goal is to determine the type of light sources that ensures a satisfactory imaging effect. For fair comparisons, all the parameters of the three types of light sources and of the point light source are same, as shown in Table 2. According to these parameters, the three-dimensional models of the light sources established by utilizing UG [31] are shown in Fig. 5. Applying the optical imaging system under the three types of light sources, respectively, the simulation results are displayed in Figs. 6–8. A comprehensive analysis of the ray-tracing, the imaging scatter and the illuminance is given as follows.

TABLE 2. Light source parameters.

Parameter	Value
Position	(0, 0, (0-15)) cm
Luminous flux	46 Lumen
Number of ray	20000
Scattering angle	40 deg
Scattering type	Lambert

To intuitively show the result of ray-tracing, 200 rays are first previewed for each light source. Fig. 6 shows the number of rays which arrive at the image receiver from the point light source is much more than that from other three light sources. The complete result of ray-tracing of 20000 rays is
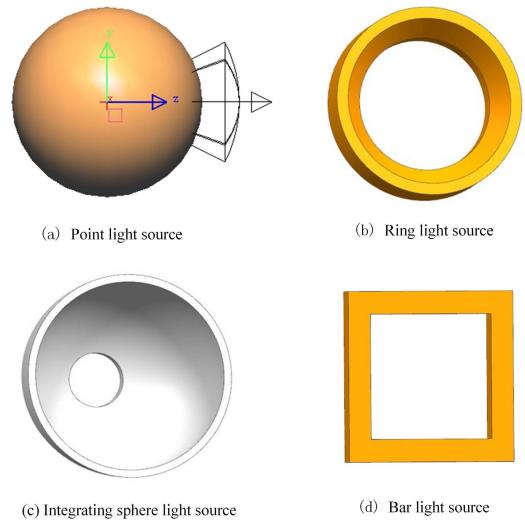

(a) Point light source

(b) Ring light source

(c) Integrating sphere light source

(d) Bar light source

FIGURE 5. Three-dimensional models of light sources.

(a) point light source

(b) ring light source

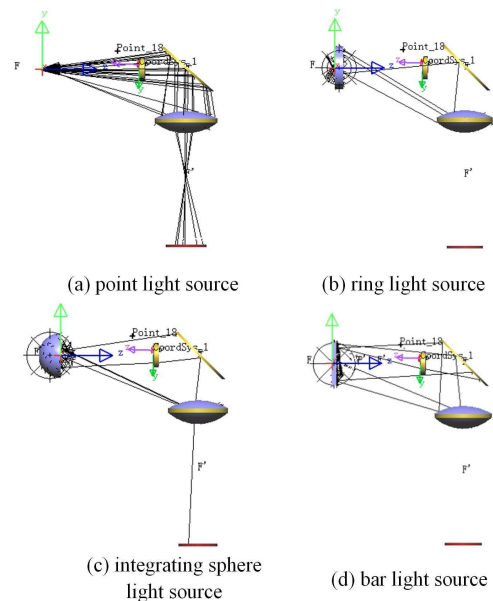(c) integrating sphere light source

(d) bar light source

FIGURE 6. Results of ray-tracing.

provided in Table 3, where N_r denotes the number of rays; D_1 represents the density of rays in defective regions; and D_2 stands for the density of rays in normal regions. The result is consistent with that of observation. The imaging scatters on the image receivers are displayed in Fig. 7. As seen, a complete imaging profile of the defect is presented under the point light source, but the image of the defect fails to be found under other light sources. The above results are consistent with the result of the density distribution of rays in Table 3. The illuminance on the image receivers is displayed in Fig. 8. It is not difficult to find that the average illuminance using the point light source is greater than 10 Lux and that using other light sources is about 1 Lux.

According to the above results, it is concluded that a satisfactory imaging effect is obtained by using the point light

TABLE 3. Number and density of rays on image receiver.

Type of light source	N_r	D_1	D_2
Point light source	1327	1.13%	6.64%
Ring light source	208	1.02%	1.04%
Integrating sphere light source	64	0.31%	0.32%
Bar light source	178	0.89%	0.89%

(a) point light source   (b) ring light source

(c) integrating sphere light source   (d) bar light source

FIGURE 7. Results of imaging scatter.

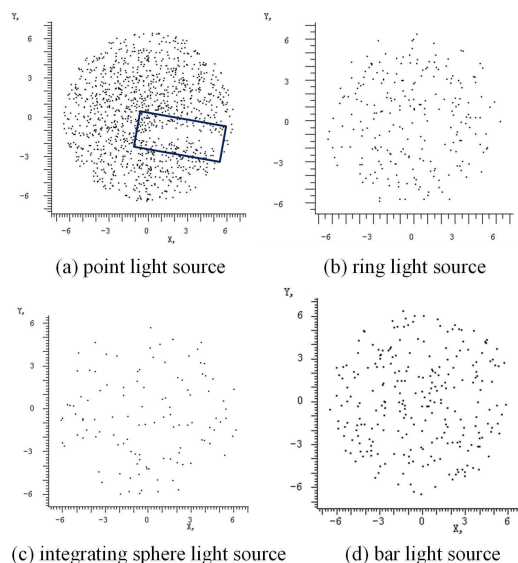(a) point light source   (b) ring light source

(c) integrating sphere light source   (d) bar light source
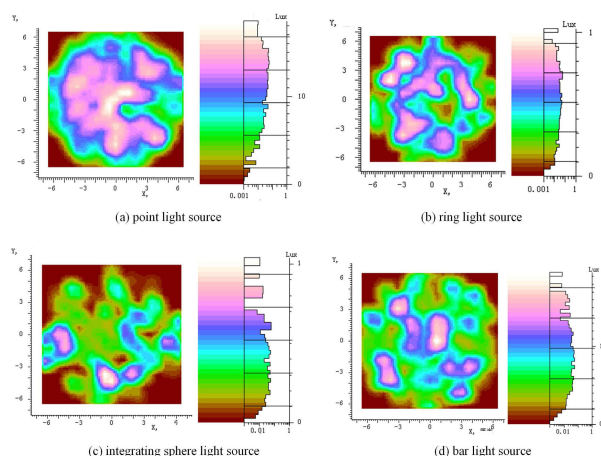
FIGURE 8. Results of illuminance.

source, among the ring light source, the integrating sphere light source, the bar light source and the point light source. This provides an important reference for the subsequent experiment.

IV. EXPERIMENTAL STUDY
In this section, an LED point light source is used for dispersed defects detection. Referring to Fig. 1, the experimental setup for the detection of the dispersed defects is built. It consists

of a point light source, an imaging screen, a camera, a light source controller, a computer, and some parts for mechanical support, as shown in Fig. 9. The support is set up by an aluminum profile and covered by the dark cloth to block out the ambient lights. To ensure sufficient illuminance in the system, the point light source (OPT-PIG0803-W, OPT, China) is connected to an adjustable light controller (OPT-APA0405-1, OPT, China), which is installed about 70 cm above the detected eyeglass. In the reverse direction, the imaging screen is placed under the eyeglass, with the distance of 10 cm. The camera (MER-503-20GM-P, IMAVISION, China) with lens (M1214-MP2, Computar, Japan) is fixed on the bottom of the frames and connected to an industrial computer through an Ethernet interface. It points to the white imaging screen to capture images under the LED light source, and the distance between the camera and the imaging screen is 15.3 cm. The acquired digital images are stored in the memory of
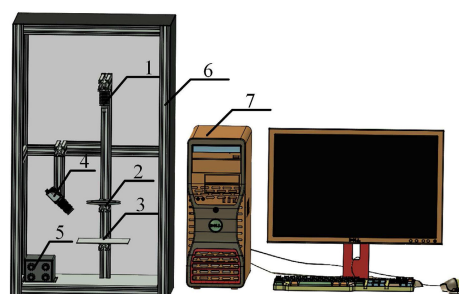
(a) Schematic diagram

(b) Physical prototype

FIGURE 9. Experimental setup for dispersed defects detection. 1. Point light source; 2. Eyeglass support; 3. Imaging screen; 4. Camera; 5. Lights controller; 6. Device support; 7. Computer.

the computer. The defect detection algorithm is programmed by Halcon 12.0 (MVTec, Germany) to detect the dispersed defects in the eyeglass.

160 gray-scale images with the resolution of 2448 × 2044 pixels are acquired from different samples. Due to the limited space, three of them are displayed in this paper to show the experimental results (see Fig. 10). It is observed that three types of dispersed defects, i.e., watermark, fog and resin streak, are clearly presented, which are marked in red. It is also found that the regions with watermark are always brighter than the normal regions, whereas the fog and resin streak regions are darker. Moreover, the gray-scale values of the acquired images vary with its thickness and diopter, and there exit a few small dark regions in the acquired images, caused by dirt and dust. However, compared with the defective eyeglass, the gray-scale values of the normal eyeglass images are more consistent due to the isotropy material.

The background in the acquired image, including the eyeglass support and the imaging plate, needs to be removed. This is achieved by using (1)–(5), and the results are exhibited in Fig. 11. Applying the region segmentation algorithm for 160 eyeglasses, the experimental results show that the background removal rate is 100%, which provides a foundation for the subsequent defect detection. The comparison between Figs. 11 and 12 reveals that the contrast between the normal region and the defective region is improved by using (6) and (7). According to (8)–(14), the detection results for dispersed defects are given in Fig. 13.

The validity of the proposed algorithm for detection of dispersed defects is further verified. The actual detection time of each sample is depicted in Fig. 14. The average detection detection time is 0.636s. The detailed data information and
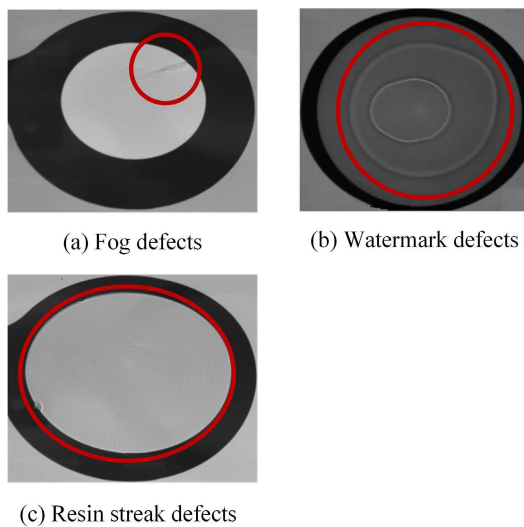

(a) Fog defects   (b) Watermark defects

(c) Resin streak defects

FIGURE 10. Images of resin eyeglass with dispersed defects.

(a) Fog defects   (b) Watermark defects

(c) Resin streak defects

FIGURE 12. Gray linear transformation of the eyeglass.

(a) Fog defects   (b) Fog Watermark defects

(c) Resin streak defects

FIGURE 11. Region segmentation of the eyeglass.

(a) Fog defects   (b) Watermark defects
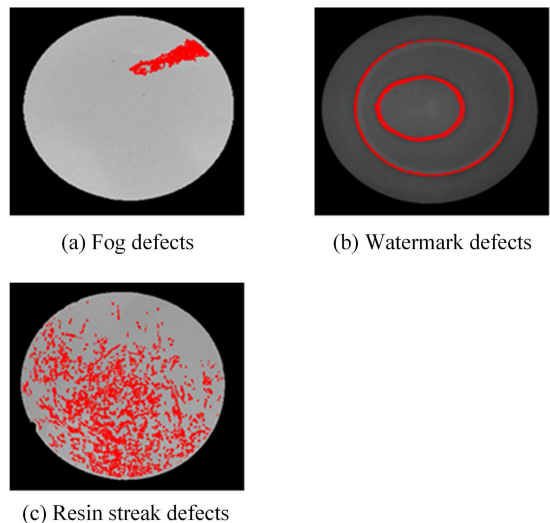
(c) Resin streak defects

FIGURE 13. Detection results of dispersed defects.
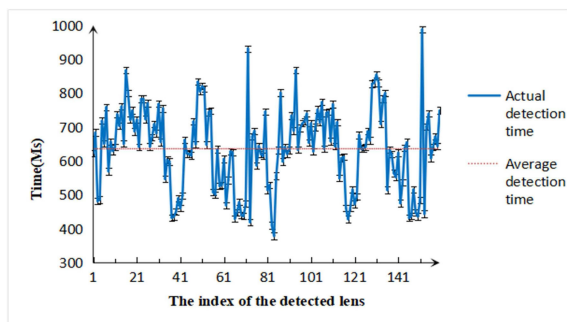
FIGURE 14. Detection time.

TABLE 4. Testing results.

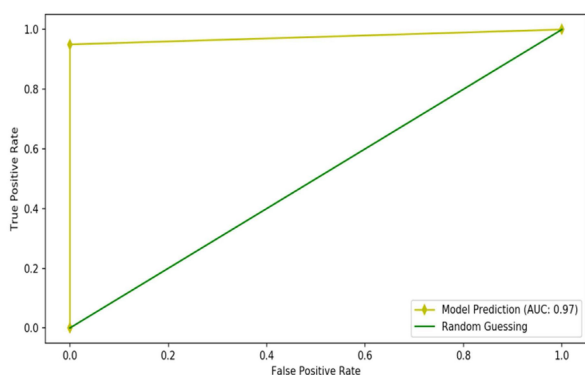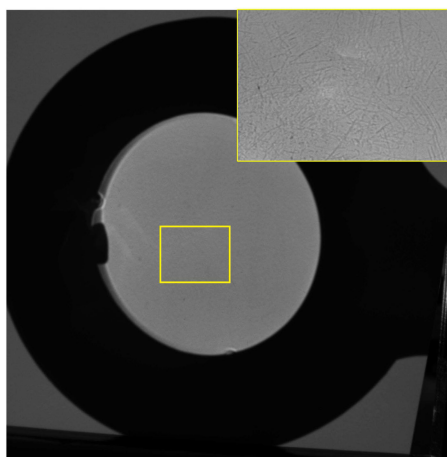|	Defective eyeglass	Normal eyeglass
Number	80	80
Detection accuracy	95%	100%

FIGURE 15. ROC curve.

FIGURE 16. Missing alarm of defective eyeglass.

the testing results are presented in Table 4. By these results, it is computed that the detection accuracy for both defective eyeglasses and normal eyeglasses of the proposed algorithm is 97.5%. Both the detection time and the detection accuracy satisfy the requirements for online detection of dispersed defects.

The receiver operating characteristic curve is shown in Fig. 15. As seen, the true-negative rate of the defective eyeglass detection is 0.95, and the area under the curve is 0.97, which illustrate that the proposed method is with a high true-positive rate and a high true-negative rate. Besides, the reason of missing alarms is explained as follows. The missing alarms of the four eyeglasses with resin streak defects are caused by the low imaging contrast between the defective region and the normal region, as shown in Fig. 16. Although a higher contrast can be obtained by the image enhancement technique, the effect of noise is aggravated. Therefore, the optimization of the imaging system such as the material of the imaging screen deserves future research.

V. CONCLUSION

The current methods to detect dispersed defects in the resin eyeglass rely on manual detection, which inevitably impairs eyes and leads to frequent false-negative detection. Motivated by this, an automatic detection strategy based on the machine vision technology is developed in this paper. An optical imaging system is first designed to show the gray-scale gradient difference between defects and the normal region in eyeglass, which is caused by the difference of refractivity. Then some simulation tests are carried out to pick out a suitable light source matching with the optical imaging system. An experimental setup is further built to acquire a clear image with a distinct gray-scale gradient difference between the normal and defective regions, by which an image processing algorithm is developed. The experimental results illustrate that the detection accuracy and the average detection time of the proposed approach not only meet the requirements for online detection but also are better than that of the manual detection method.

DISCLOSURE STATEMENT

The authors declare that they have no known competing financial interests or personal relationships that could have appeared to influence the work reported in this article.

REFERENCES

[1] B. A. Holden, T. R. Fricke, D. A. Wilson, M. Jong, K. S. Naidoo, P. Sankaridurg, T. Y. Wong, T. J. Naduvilath, and S. Resnikoff, "Global prevalence of myopia and high myopia and temporal trends from 2000 through 2050," *Ophthalmology*, vol. 123, no. 5, pp. 1036–1042, May 2016.

[2] B. Rust, O. Tsaponina, and M. Maniruzzaman, "Recent innovations in additive manufacturing across industries: 3D printed products and FDA's perspectives," in *3D and 4D Printing in Biomedical Applications*. Hoboken, NJ, USA: Wiley, 2018, ch. 17, pp. 443–462, doi: 10.1002/9783527813704.ch17.

[3] W. Du, L. Tan, Y. Zhang, H. Yang, and H. Chen, "Dynamic rheological investigation during curing of a thermoset polythiourethane system," *Int. J. Polym. Sci.*, vol. 2019, pp. 1–10, Mar. 2019.

[4] J. Sun, C. Li, X.-J. Wu, V. Palade, and W. Fang, "An effective method of weld defect detection and classification based on machine vision," *IEEE Trans Ind. Informat.*, vol. 15, no. 12, pp. 6322–6333, Dec. 2019.

[5] C. Li, G. Gao, Z. Liu, D. Huang, and J. Xi, "Defect detection for patterned fabric images based on GHOG and low-rank decomposition," *IEEE Access*, vol. 7, pp. 83962–83973, 2019.

[6] J. Yang, S. Li, Z. Wang, and G. Yang, "Real-time tiny part defect detection system in manufacturing using deep learning," *IEEE Access*, vol. 7, pp. 89278–89291, 2019.

[7] F. Rainer, "Mapping and inspection of damage and artifacts in large-scale optics," in *Laser-Induced Damage in Optical Materials: 1997*, G. J. Exarhos, A. H. Guenther, M. R. Kozlowski, and M. J. Soileau, Eds., vol. 3244. Bellingham, WA, USA: SPIE, 1998, pp. 272–281, doi: 10.1117/12.307019.

[8] A. Conder, J. Chang, L. Kegelmeyer, M. Spaeth, and P. Whitman, "Final optics damage inspection (FODI) for the national ignition facility," *Proc. SPIE*, vol. 7797, Aug. 2010, Art. no. 77970P.

[9] Y.-L. Deng, S.-P. Xu, H.-Q. Chen, Z.-H. Liang, and C.-L. Yu, "Inspection of extremely slight aesthetic defects in a polymeric polarizer using the edge of light between black and white stripes," *Polym. Test.*, vol. 65, pp. 169–175, Feb. 2018.

[10] C.-F.-J. Kuo, C.-Y. Lai, C.-H. Kao, and C.-H. Chiu, "Integrating image processing and classification technology into automated polarizing film defect inspection," *Opt. Lasers Eng.*, vol. 104, pp. 204–219, May 2018.

[11] Z.-C. Yuan, Z.-T. Zhang, H. Su, L. Zhang, F. Shen, and F. Zhang, "Vision-based defect detection for mobile phone cover glass using deep neural networks," *Int. J. Precis. Eng. Manuf.*, vol. 19, no. 6, pp. 801–810, Jul. 2018.

[12] M. Chang, B.-C. Chen, J. L. Gabayno, and M.-F. Chen, "Development of an optical inspection platform for surface defect detection in touch panel glass," *Int. J. Optomechatronics*, vol. 10, no. 2, pp. 63–72, Mar. 2016.

[13] V. Trivedi, M. Joglekar, S. Mahajan, N. Patel, V. Chhaniwal, B. Javidi, and A. Anand, "Digital holographic imaging of refractive index distributions for defect detection," *Opt. Laser Technol.*, vol. 111, pp. 439–446, Apr. 2019.

[14] Z. Cen, Z. Chen, and X. Li, "Diffraction method for inspecting the defects of lenses with various curvature," *Proc. SPIE*, vol. 10815, Nov. 2018, Art. no. 108150P.

[15] S. A. Bel'kov, I. N. Voronich, A. S. Gubkin, V. N. Derkach, I. N. Derkach, A. V. Dobikov, V. O. Lashchuk, and V. A. Shchenikov, "Automated system for finding flaws in optical components," *J. Opt. Technol.*, vol. 86, no. 5, pp. 306–309, Aug. 2019.

[16] R. E. Wijesinghe, K. Park, Y. Jung, P. Kim, M. Jeon, and J. Kim, "Industrial resin inspection for display production using automated fluid-inspection based on multimodal optical detection techniques," *Opt. Lasers Eng.*, vol. 96, pp. 75–82, Sep. 2017.

[17] Y. Hongbing, Z. Xueliang, M. Guidian, Z. Xiangbo, L. Yaru, G. Yuan, Y. Wenlong, and G. Jinan, "Research on lens-defects type recognition based on image processing," *Laser Optoelectronics Progr.*, vol. 50, no. 11, 2013, Art. no. 111003.

[18] G. Pan, Y. Xie, C. Xu, M. Xun, Y. Dong, J. Deng, H. Chen, and J. Sun, "Dependence of beam quality on optical intensity asymmetry in in-phase coherently coupled VCSEL array," *IEEE J. Quantum Electron.*, vol. 54, no. 3, pp. 1–6, Jun. 2018.

[19] R. C. Gonzalez and R. E. Woods, *Digital Image Processing*, 3rd ed. Upper Saddle River, NJ, USA: Prentice-Hall, 2006.

[20] Y. Xu, J. Wen, L. Fei, and Z. Zhang, "Review of video and image defogging algorithms and related studies on image restoration and enhancement," *IEEE Access*, vol. 4, pp. 165–188, 2016.

[21] S. Huang, Z. Peng, Z. Wang, X. Wang, and M. Li, "Infrared small target detection by density peaks searching and maximum-gray region growing," *IEEE Geosci. Remote Sens. Lett.*, vol. 16, no. 12, pp. 1919–1923, Dec. 2019.

[22] H. Zhao, B. He, Z. Ding, K. Tao, T. Lai, H. Kuang, R. Liu, X. Zhang, Y. Zheng, J. Zheng, and T. Liu, "Automatic lumen segmentation in intravascular optical coherence tomography using morphological features," *IEEE Access*, vol. 7, pp. 88859–88869, 2019.

[23] G. Luo, Y. Zhu, Z. Weng, and Z. Li, "A disocclusion inpainting framework for depth-based view synthesis," *IEEE Trans. Pattern Anal. Mach. Intell.*, to be published.

[24] A. Yousefi, A. K. Gillespie, J. A. Guidera, M. Karlsson, L. M. Frank, and U. T. Eden, "Efficient decoding of multi-dimensional signals from population spiking activity using a Gaussian mixture particle filter," *IEEE Trans. Biomed. Eng.*, vol. 66, no. 12, pp. 3486–3498, Dec. 2019.

[25] H. K. Verma and S. Pal, "Modified sigmoid function based gray scale image contrast enhancement using particle swarm optimization," *J. Inst. Eng., B*, vol. 97, no. 2, pp. 243–251, Jan. 2015.

[26] T. Matić, I. Aleksi, Ž. Hocenski, and D. Kraus, "Real-time biscuit tile image segmentation method based on edge detection," *ISA Trans.*, vol. 76, pp. 246–254, May 2018.

[27] A. Halder, A. Sarkar, and S. Ghose, "Adaptive histogram equalization and opening operation-based blood vessel extraction," in *Soft Computing in Data Analytics*. Singapore: Springer, 2019, pp. 557–564.

[28] M. J. Klaiber, D. G. Bailey, and S. Simon, "A single-cycle parallel multi-slice connected components analysis hardware architecture," *J. Real-Time Image Process.*, vol. 16, no. 4, pp. 1165–1175, Jun. 2016.

[29] Y. Lyu, Q. Yang, and S. Gao, "Application study of optical modeling and analysis software virtual lab in optical design," *Acta Microscopica*, vol. 28, no. 4, pp. 1–9, 2019.

[30] X. Guo, J. Tang, J. Li, C. Shen, and J. Liu, "Attitude measurement based on imaging ray tracking model and orthographic projection with iteration algorithm," *ISA Trans.*, vol. 95, pp. 379–391, Dec. 2019.

[31] H. Li, Y. Zheng, X. Wu, and Q. Cai, "3D model generation and reconstruction using conditional generative adversarial network," *Int. J. Comput. Intell. Syst.*, vol. 12, no. 2, pp. 697–705, 2019.

WEI DING received the B.E., B.S., and Ph.D. degrees in mechanical engineering from Jiangsu University, Zhenjiang, China, in 2007, 2012, and 2017, respectively.

From 2017 to 2018, she was with the Faculty of Electrical Engineering and Automation, Changshu Institute of Technology. She is currently a Postdoctoral Research Fellow with the Faculty of Engineering and the Built Environment, Institute for Intelligent Systems, University of Johannesburg. Her current research interests include machine vision and pattern recognition.

QINGGUO WANG received the B.Eng. degree in chemical engineering, the M.Eng. degree in industrial automation, and the Ph.D. degree in industrial automation from Zhejiang University, Hangzhou, China, in 1982, 1984, and 1987, respectively.

He held the Alexander-von-Humboldt Research Fellowship of Germany, from 1990 to 1992. From 1992 to 2015, he was with the Department of Electrical and Computer Engineering, National University of Singapore, where he became a Full Professor, in 2004. He is currently a Distinguished Professor with the Institute for Intelligent Systems, University of Johannesburg, Johannesburg, South Africa. He holds A-rating from the National Research Foundation of South Africa. He is currently a member of the Academy of Science of South Africa. He has authored/coauthored approximately 300 international journal papers and seven research monographs. His current research interests include modeling, estimation, prediction, control, optimization, and automation for complex systems, including but not limited to, industrial and environmental processes, new energy devices, defense systems, medical engineering, and financial markets.

Prof. Wang received about 13 000 citations with H-index of 63. He is currently the Deputy Editor-in-Chief of ISA *Transactions*, USA.

JIANFENG ZHU received the B.Eng. degree in mechanical engineering and automation from the Taihu University of Wuxi, Wuxi, China, in 2016, the M.Eng. degree from the School of Mechanical Engineering, Jiangsu University, Zhenjiang, China, in 2019, where he is currently pursuing the Ph.D. degree at the School of Mechanical Engineering.

His current research interests include machine vision and intelligent inspection in industry.

• • •